International Journal of Hydrogen Energy 71 (2024) 763–774

Contents lists available at ScienceDirect

International Journal of Hydrogen Energy

journal homepage: www.elsevier.com/locate/he

Transition metal polyoxometalates with reduced graphene oxide for high-performance air-electrode of metal-air batteries

Filipe M.B. Gusmão [a], Teodora Đurić [b], Jadranka Milikić [b], Kristina Radinović [b], Diogo M.F. Santos [a], Dalibor Stanković [c,d], Biljana Šljukić [a,b,*]

[a] Center of Physics and Engineering of Advanced Materials, Laboratory for Physics of Materials and Emerging Technologies, Chemical Engineering Department, Instituto Superior Técnico, Universidade de Lisboa, 1049–001 Lisbon, Portugal
[b] University of Belgrade, Faculty of Physical Chemistry, Studentski trg 12–16, 11158, Belgrade, Serbia
[c] University of Belgrade, Faculty of Chemistry, Studentski trg 12–16, 11158, Belgrade, Serbia
[d] "VINČA" Institute of Nuclear Sciences – National Institute of the Republic of Serbia, University of Belgrade, Mike Petrovića Alasa 12-14, 11000, Belgrade, Serbia

ARTICLE INFO

Keywords:
Transition metals
Polyoxometalates
Reduced graphene oxide
Oxygen evolution reaction
Oxygen reduction reaction
Metal-air batteries

ABSTRACT

The potential of polyoxometalates (POMs) as alternatives to noble metal-based bifunctional electrocatalysts for air electrode, i.e., for oxygen evolution reaction (OER) and oxygen reduction reaction (ORR), was analyzed herein. Five POMs containing transition metal (Mn, Fe, Co, Ni, or Cu) were prepared and combined with reduced graphene oxide (rGO). Kenning structure of POMs with nanolamellae-like morphology and multi-layered graphene sheets of rGO were confirmed by X-ray diffraction, Fourier-transform infrared spectroscopy, scanning electron microscopy with energy dispersive X-ray spectroscopy, transmission electron microscopy and Raman spectroscopy analysis. Different POM:rGO ratios were tested to optimize the composition, and a ratio of 1:5 Ni-POM:rGO was found to be the most electrocatalytically active for OER (Tafel slope as low as 42 mV dec^{-1}, overpotential at 10 mA cm^{-2} of 354 mV and current density at 400 mV overpotential as high as 83.4 mA cm^{-2}), notably better than IrO_2. As for ORR, Co-POM/rGO carried the lowest Tafel slope of 165 mV dec^{-1}, half-wave potential of 0.711 V and a mixed 2- and 4-electron ORR mechanism. Moreover, these non-precious metal electrocatalysts showed stability in alkaline media with no change in their structure.

1. Introduction

Climate change is already taking its toll. At the 77th session of the UN General Assembly (UNGA 77) held in New York City in 2022, climate action was pointed out as a priority of every government. Global greenhouse gas emissions must be reduced by 45% by 2030, allowing net zero emissions to be reached by 2050. Despite all evidence that actions must be taken, greenhouse gas emissions are expected to increase by around 14% this decade [1]. Developing and putting industrial energy storage and production options that do not emit greenhouse gases in place should be prioritized for all developed countries. Significant breakthroughs have been made in renewable energy production, a crucial part of the solution to curb greenhouse emissions, with substantial investments already in place in many European countries. Nevertheless, sustainable renewable energy production relies on efficient energy storage, as its output varies widely throughout the day and the year. Efficient energy storage guarantees that this energy becomes available consistent with demand (see Scheme 1).

Metal-air batteries (MABs) present very high specific capacity and energy density, ideal for modern energy applications such as electric vehicles. Right now, the biggest drawback of MABs is their low cycle life, resulting from metal oxidation at the anode, making rechargeable designs challenging to produce. Nevertheless, recent advances, such as using ionic liquids and solid-state electrolytes, have shown that the mentioned shortcomings can be solved [2,3].

As oxygen evolution reaction (OER) has slow kinetics, it requires high overpotentials for reasonable currents to develop [4,5]. The electrocatalysts typically used to reduce the electrical uptake of this reaction are made of high-cost and scarce metals such as lanthanum [6], iridium and ruthenium [7]. The best-performing low-cost catalysts typically operate in current ranges below 100 mA cm^{-2}, which are unsuitable for industrial use. The electrocatalyst must be bifunctional for rechargeable

* Corresponding author. Center of Physics and Engineering of Advanced Materials, Laboratory for Physics of Materials and Emerging Technologies, Chemical Engineering Department, Instituto Superior Técnico, Universidade de Lisboa, 1049–001 Lisbon, Portugal.
E-mail address: biljana.paunkovic@tecnico.ulisboa.pt (B. Šljukić).

https://doi.org/10.1016/j.ijhydene.2024.05.229
Received 13 February 2024; Received in revised form 3 May 2024; Accepted 14 May 2024
Available online 23 May 2024

MABs, i.e., active for OER and oxygen reduction reaction (ORR). ORR mechanism has two possible pathways: two-electron and four-electron pathways. The four-electron pathway is preferred in energy conversion and storage systems, as there is higher electricity production and no generation of H_2O_2, a powerful oxidant that may damage some of the cell components. To this end, platinum is the most commonly used electrocatalyst for ORR, another high price noble metal that hinders its use in industrial applications [8,9].

Marini et al. [10] reported the challenges of designing bifunctional electrocatalysts. They synthesized a ternary material based on $(C)_x(MnO_2)_y(Ni/NiO)_{100-x-y}$ and studied different ratios of each component. As the Ni/NiO amount increased, the material's activity for OER also increased, but this came at the cost of its activity for ORR. This example conveys the difficulty in the production of efficient bifunctional electrocatalysts.

Polyoxometalates (POMs) with abundant metal sources, have shown high thermal stability and good resistance to oxidative decomposition, making them excellent options for electrocatalysis [11]. Moreover, their elemental composition, valence state, and skeleton structure can be tuned (see below). Although POM salts are mostly insulators, it is now possible to link POMs to conductive and high-surface-area materials through covalent or non-covalent means [12], using nanostructured conductive carbons such as carbon nanotubes (CNTs) or graphene [13]. "Wiring" POMs to conductive organic polymers has also been suggested as a way to overcome the issue of their low conductivity [14]. It seems possible, then, to overcome POMs' low conductivity and produce a reliable electrical connection between the POM as the reaction center and other parts of the device, thus enabling the technological use of POMs in electrical devices. POMs have exhibited the potential for multi-electron transfer, with their unique redox properties allowing the reversible uptake of up to 24 electrons per cluster unit (for instance, $[PMo_{12}O_{40}]^{3-}$), which has been observed in the solid state [15].

POMs represent a class of metal–oxygen cluster compounds with a basic building unit MO_x (x = 4, 5, 6, …), where M is typically a high-valent transition metal (TM) such as W, Mo, V, Nb, Ta, etc. TM can be replaced by metal ions of almost any element, i.e., d-, f-, ds-, and p-block of the periodic table. Moreover, the central atom in POM anion can be replaced by different heteroatoms (X), metal or non-metal, including Si, P, B, Ge, S, Se, Ga, etc. Most studied classes of POMs include the Anderson-Evans $[XM_6O_{24}]^{n-}$, Lindqvist $[M_6O_{19}]^{n-}$, Keggin $[XM_{12}O_{40}]^{n-}$, and Dawson $[X_2M_{18}O_{62}]^{n-}$ structural classes [16,17]. The negative charge is balanced by Li^+, Na^+, K^+, Cs^+ counter-cations or less frequently the alkali-earth cations. Kegging structural class especially offers great variety of composition, charge, and redox states that are accessible with comparatively minor changes to the molecular structure. Furthermore, chemical modification of the POM structure can manipulate their electrochemical properties, such as redox potentials and the number of exchanged electrons. One of the available methods is incorporating redox-active metal centers in the POMs. Metal functionalization can also generate coordinative substrate binding sites for electrochemical and electroanalytical applications [18,19]. Finally, there is already a large body of knowledge about these materials, and applications in materials and medical sciences are currently in place, supporting the potential scalability of these materials to industrial levels [20–23].

POMs have thus interesting properties for OER and ORR electrocatalysis, with potentially good activity, low cost, and scalability [11,17,24]. POMs have often been explored in form of composites with MOFs, etc. [25–28]. POM-based electrocatalysts with different metals (noble metal ruthenium as well as non-noble metals manganese, iron, cobalt, nickel, and copper) have been explored as OER catalysts in alkaline media needing overpotential to reach 10 mA cm^{-2} in a broad 205–580 mV range and Tafel slope in 38–235 mV dec^{-1} range [11]. POM-based electrocatalysts studied for ORR again included those containing Co, Ni and Fe grafted on carbons with ORR proceeding by mixed 2- and 4-electron mechanism or by direct 4-electron mechanism [11]. This study explores the use of five transition-metal-based POMs containing Co, Ni, Mn, Cu and Fe combined with reduced graphene oxide expecting to overpass the so-far-reported activity and overcome instability (solubility) as a critical issue for POM use in electrocatalysis. The synthesized POMs were characterized in terms of their structure, surface functionality, morphology, and atomic composition. They were tested as

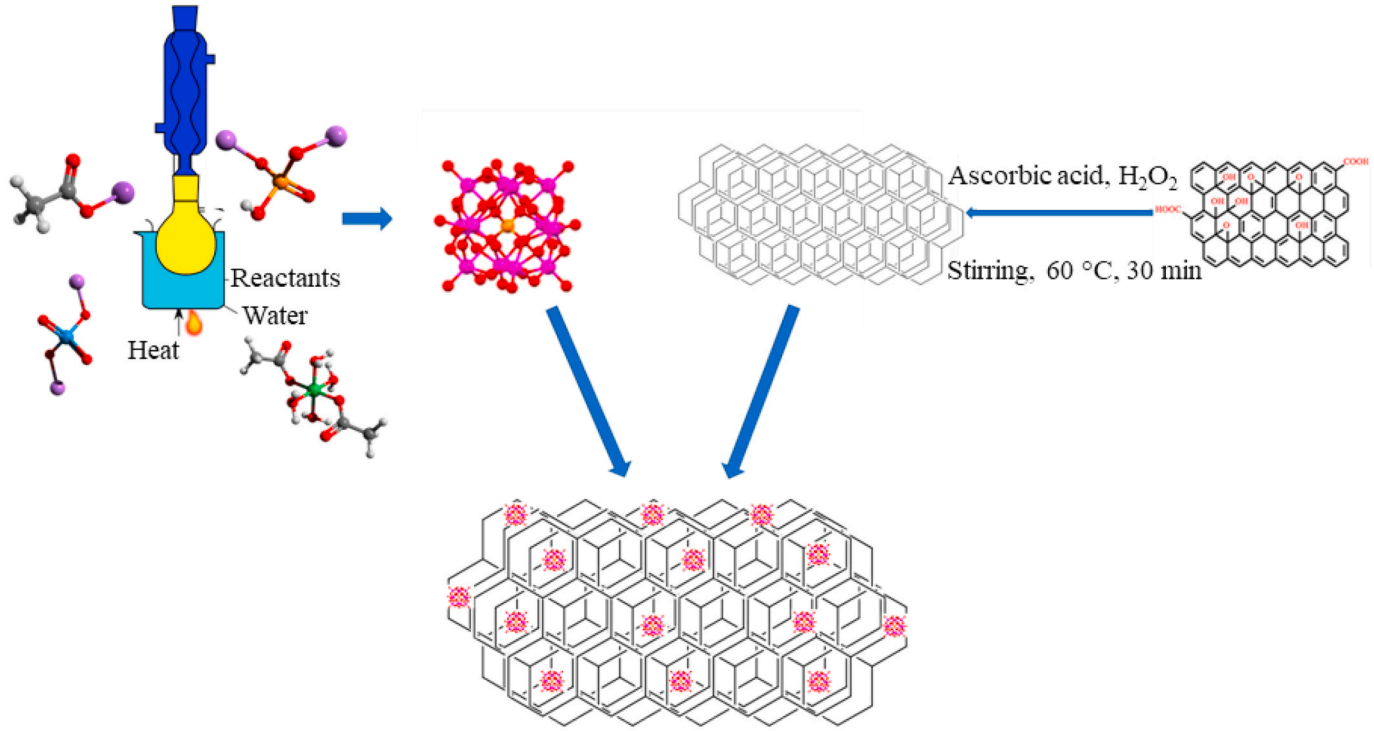

Scheme 1. The synthesis process of the POM/rGO composites.

catalysts for OER and ORR and then applied in lab-scale MABs. The results are then discussed, and their performance and cost are compared with current benchmark materials.

2. Experimental procedure

2.1. Materials and methods

All chemical used in this study were purcesed from Sigma Aldrich and used as received with no urther purification. These included graphene oxide (dispersion in H_2O), ascorbic acid (99%), hydrogen peroxide (H_2O_2, ≥30%) potassium hydroxide (KOH, 90%, flakes).

2.2. Synthesis and characterization of POM composites with rGO

POMs $K_6Na_4[X_4(H_2O)_2(PW_9O_{34})_2]\cdot 24H_2O$, where X = Ni, Mn, Cu, Co, or Fe, were synthesized using a procedure similar to the one proposed by Clemente-Juan et al. [29]. Reduced graphene oxide (rGO) was synthesized by ultrasonically treating a suspension of graphene oxide (210 mg) in distilled water (200 mL) for 1.5 h, followed by the addition of ascorbic acid (2 g). The suspension was then heated to 60 °C in a magnetic stirrer for 40 min. Next, the suspension was centrifuged, and 30% H_2O_2 was added to the obtained precipitate. This new suspension was magnetically stirred at 60 °C for 30 min. It was then centrifuged, and the obtained precipitate was dried in an oven at 120 °C for 24 h. The composites with different POM to rGO ratios (1:5, 2:4, 3:3, 4:2, 5:1) were prepared by sonicating the two components and 1 mL of ethanol for 2 h and then leaving the mixture air-drying for the ethanol to evaporate.

For the investigation of the structure of POM/rGO composite materials, X-ray diffraction (XRD) analysis was performed using a Rigaku Ultima IV diffractometer in Bragg-Brentano geometry, with Ni-filtered CuKα radiation (λ = 1.54178 Å). Diffraction data were obtained using scattering angle 2θ from 20 to 90° with a step of 0.020° and acquisition rate of 2° min^{-1}. Fourier-transform infrared (FTIR) spectroscopy analysis was carried out using a PerkinElmer GX1 spectrometer to determine the surface functional groups of the POM/rGO samples. The Raman spectrum of rGO was recorded on a DXR Raman microscope (Thermo Scientific, USA). Examination of surface morphology and determination of atomic composition was made by Phenom™ ProX Desktop (Thermo Fisher Scientific™, Waltham, MA, USA) scanning electron microscope with integrated energy-dispersive X-ray spectroscopy (SEM-EDX) detector and a Jeol JSM 7001 F (JEOL, Ltd., Japan) electron microscope. Detailed examination of surface morphology and microstructure of POM/rGO composites was done by transmission electron microscopy (TEM) analysis, a JEM-2100 analysis (JEOL, Ltd., Japan) in an operating voltage of 200 kV.

2.3. Electrocatalysis using POM/rGO composites

The activity of the prepared POM/rGO materials for OER and ORR electrocatalysis was assessed using a typical three-electrode cell with a saturated calomel electrode (SCE) as the reference, a platinum coil as the counter electrode, and POM/rGO in the form of a thin film on a glassy carbon rod substrate as the working electrode. Graphite rod was used as the counter electrode during the stability tests. Additionally, working electrodes with pure rGO and pristine POM were prepared. The measured potentials were converted to the reversible hydrogen electrode (RHE) scale. Thus, all presented potential values are vs. RHE unless otherwise stated.

Catalytic inks were prepared by sonicating POM/rGO composites (6 mg), deionized water (600 μL), ethanol (400 μL, 96%), and Nafion™ (25 μL, 0.5 wt%) for 30 min in an Emmi® - 08ST sonicator, EMAG Technologies®. The inks were pipetted onto a glassy carbon rod (0.5 cm^2), leading to a catalyst loading of 0.176 mg cm^{-2}.

All electrodes were placed in 80 mL of 1 M KOH supporting electrolyte. Electrochemical measurements were performed in a Squidstat™ potentiostat, Admiral Instruments, and an Ivium V01107 Potentiostat/Galvanostat.

Capacitance measurements were done in N_2-saturated solution, achieved by bubbling N_2 in the electrolyte solution for 15 min before the experiments and at a lower flow while running them.

OER studies were carried out by linear scan voltammetry at a scan rate of 5 mV s^{-1}, followed by electrochemical impedance spectroscopy (EIS) in the frequency range from 100 kHz to 0.1 Hz at several potentials (1.57, 1.67, and 1.77 V). ORR studies were carried out in O_2-saturated solution using cyclic voltammetry with a rotating disk electrode at 5 mV s^{-1} and electrode rotation rates of 300, 600, 900, 1200, 1800, 2400, and 3600 rpm.

3. Results and discussion

3.1. Characterization of the synthesized transition metal (TM)-POM/rGO composites

XRD patterns of all five samples show a broad peak at 2θ of 25° corresponding to the reflections from the rGO crystal planes, Fig. 1A. Characteristic peaks of POM structure are not observed in the POM/rGO composite materials because of the high POM dispersion on the rGO surface [30–33]. Fig. 1C illustrates the pristine Co-POM, where characteristic peaks of the POM structure can be seen [34,35].

FTIR spectra of POM/rGO composites reveal the four characteristic POMs' bands at 1108, 947, 881, and 802 cm^{-1}, Fig. 1D, corresponding to the frequency of P–O in the central PO_4 and W═O in the exterior WO_6, W−O_b−W, and W−O_c−W bridges, respectively [31,33,36]. The same bands are visible in the FTIR spectrum of the pristine Co-POM, Fig. 1E. Absorption rGO bands were observed at 1683, 1561, 1402, and 1038 cm^{-1}, Fig. 1D, and could be associated with C═O, C═C, C–H, and C–O, respectively [33,37]. The low intensity of rGO bands compared with the intensity of the graphene oxide (GO) absorption band results from reduced oxygen functionalities in rGO [31]. Fig. 1F shows the FTIR spectra of GO and rGO where absorption bands characteristic of GO structure, i.e., bands of C═O, C═C, C–H, and C–O groups, were seen at 1048, 1383, 1619, and 1714 cm^{-1}, respectively [33,37]. The intensity of absorption bands of rGO was somewhat lower than that of GO, as previously reported [38]. The FTIR spectra of the POM/rGO composites confirmed that POMs and rGO structures are preserved in all five samples.

Raman spectrum of rGO (Fig. 1C) displays two distinctive peaks at 1350 and 1590 cm^{-1}, corresponding to D and G bands characteristic of graphitic structure. D band originates from the changes in the aromatic rings with defects and presents amorphous structures of carbon, while G band originates from the bond stretching of all pairs of sp2 atoms and presents the graphitic structure of carbon. Thus, D/G ratio, reflecting the size of sp2 domain of graphene sheets with sp3 and sp2 bonds, determined to be ~1 suggests the existence of defects (most likely edge defects). Moreover 2D bands are observed at 2720 and 3200 cm^{-1}. It has been previously reported that the G and 2D bands of single-layer graphene sheets are typically observed at 1585 and 2679 cm^{-1}, respectively, but shifting to lower and higher wavenumbers by 6 and 19 cm^{-1}, respectively, for multi-layer graphene sheets [39,40]. The herein observed 2D band at 2720 cm^{-1} indicates multi-layer graphene sheets (also observed in TEM images). Moreover, the 2D/G ratios of >1.6, 0.8, 0.30 and 0.07 is usually observed for single-, double-, triple- and multi-(>4) layer graphene sheets, respectively [39,40]. Herein, the 2D/G ratios of ~0.13 and ~0.07 confirm presence of multi-layer graphene sheets.

SEM images of the POM/rGO composites, Fig. 2A,C–F, clearly show similar morphology of all five samples, whereas Fig. 2B illustrates the morphology of the pristine Co-POM sample. Apparent differences in the morphology of the POM/rGO samples compared with pristine POM could be noticed. The presence of metal (Ni, Co, Mn, Cu, or Fe) within

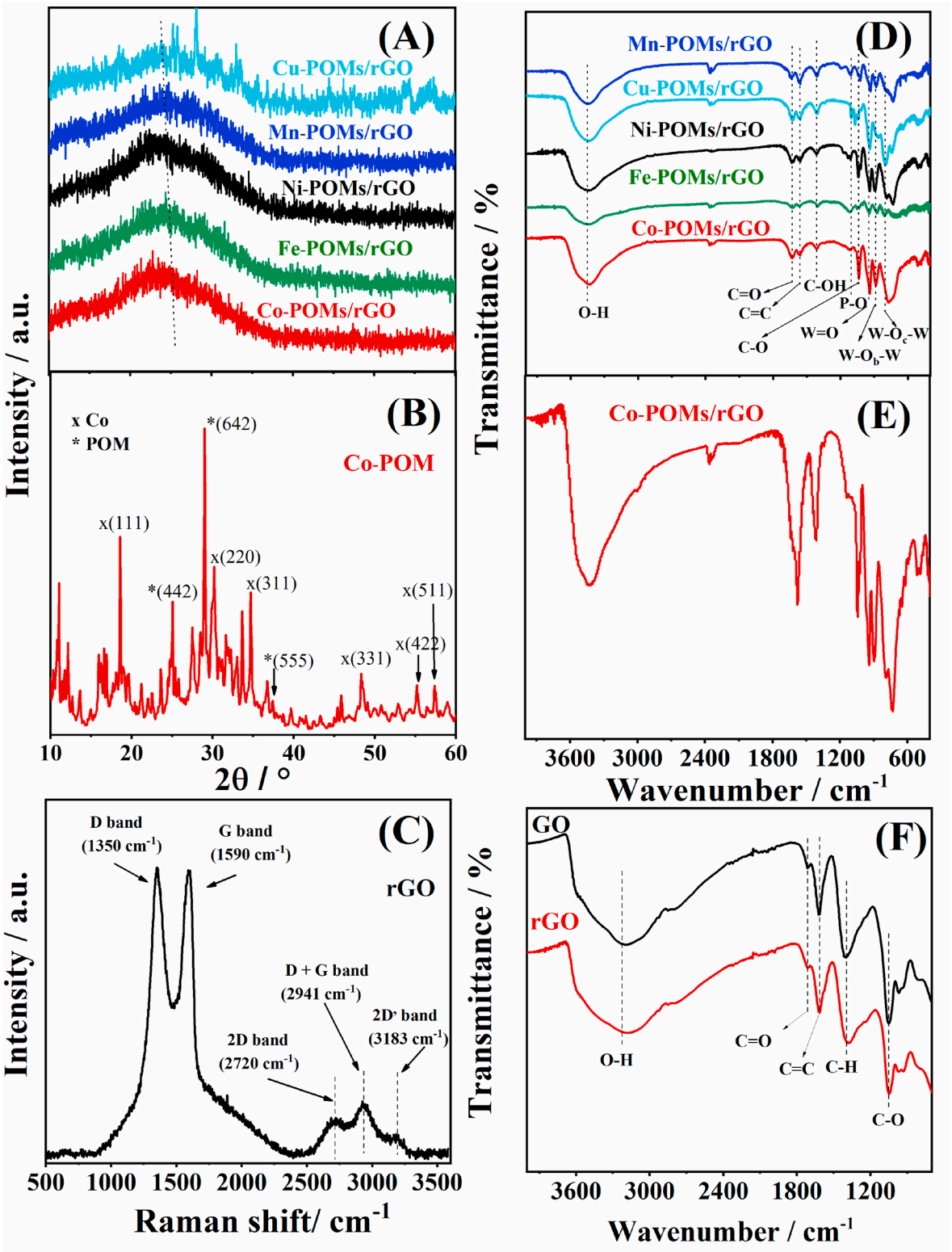

Fig. 1. XRD patterns (A) and FTIR spectra (D) of the studied TM-POM/rGO electrocatalysts and the XRD pattern (B) and FTIR spectrum (E) of pristine Co-POM electrocatalyst. Raman spectrum of rGO (C) and FTIR spectra of GO and rGO (F).

the corresponding POM/rGO composite structure was confirmed by SEM-EDS analysis; Fig. 2A inset illustrates the case of Co-POM/rGO. Furthermore, elemental mapping revealed uniform metal distribution in the corresponding composite and elements originating from the POM/rGO structure (W, Na, K, C, and O); Fig. 2g1-g6 illustrates the case of Co-POM/rGO.

Morphology of TM-POM/rGO was further observed by TEM, Fig. 3. Characteristic rGO morphology could be observed comprising some single, but mostly few sheets (lighter and darker grey sheets) [41], while TM-POMs displayed nanolamellae-like morphology. Clearly seen edge of rGO and TM-POMs suggested strong POM nanolamellae – rGO sheet interaction [42,43].

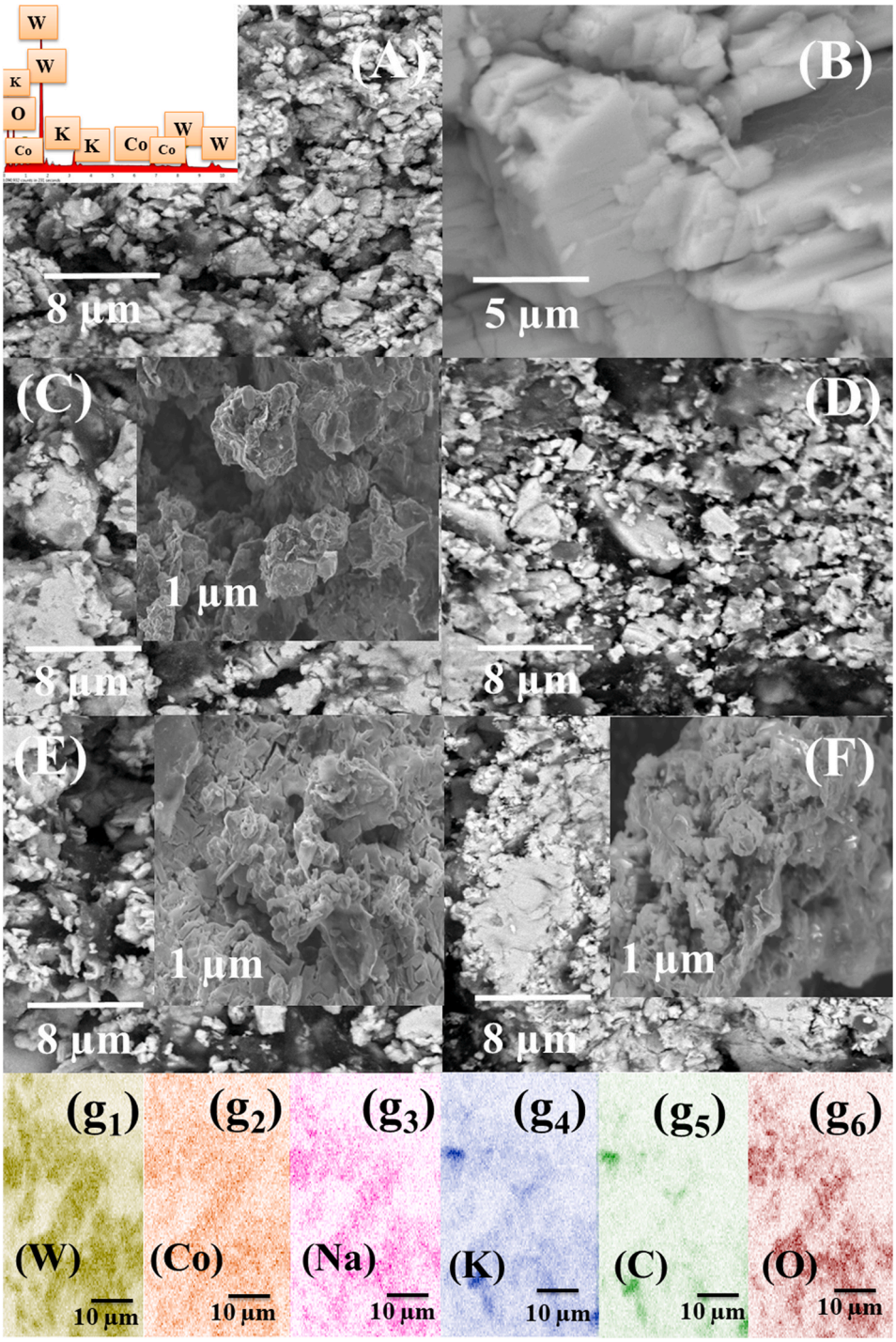

Fig. 2. SEM images of Co-POM/rGO with its EDS spectrum in inset (A), pristine Co-POM (B), Fe-POM/rGO (C), Mn-POM/rGO (D), Ni-POM/rGO (E), and Cu-POM/rGO (F), and the elemental mapping of Co-POM/rGO (g1-g6).

3.2. Study of POM/rGO composites as electrocatalysts for OER

Linear scan voltammograms (LSVs) of five studied POM/rGO (5:1) composites were first recorded under OER polarization conditions in 1 M KOH, Fig. 4A. The LSVs immediately reveal the highest current density within the studied potential range in the case of Ni-POM/rGO and negligible current density in the case of Cu-POM/rGO. Onset potential (E_{onset}), i.e., the potential to reach a current density of 1 mA cm^{-2}, was found to increase in the order Ni-POM/rGO (1.553 V) < Co-POM/rGO (1.605 V) < Fe-POM/rGO (1.615 V) < Mn-POM/rGO (1.656 V), Table 1. Furthermore, Ni-POM/rGO exhibited the lowest overpotential to reach a current density of 10 mA cm^{-2} (η_{10}) of 0.366 V, which was approximately 54 mV and 85 mV lower than that of Co-POM/rGO (0.420 V) and Fe-POM/rGO (0.451 V), respectively, Table 1. Mn-POM/rGO and Cu-POM/rGO did not reach a current density of 10 mA cm^{-2} within the studied potential range. Furthermore, the current density at an overpotential of 400 mV (j_{400}) was found to decrease in the order Ni-POM/rGO (21.8 mA cm^{-2}) > Co-POM/rGO (3.1 mA cm^{-2}) > Fe-POM/rGO (1.7 mA cm^{-2}) > Mn-POM/rGO (0.4 mA cm^{-2}) > Cu-POM/rGO (0.2 mA cm^{-2}), Table 1.

Next, Tafel analysis was performed to gain further insight into the electrocatalysts' properties and activity for OER catalysis, Fig. 4A inset.

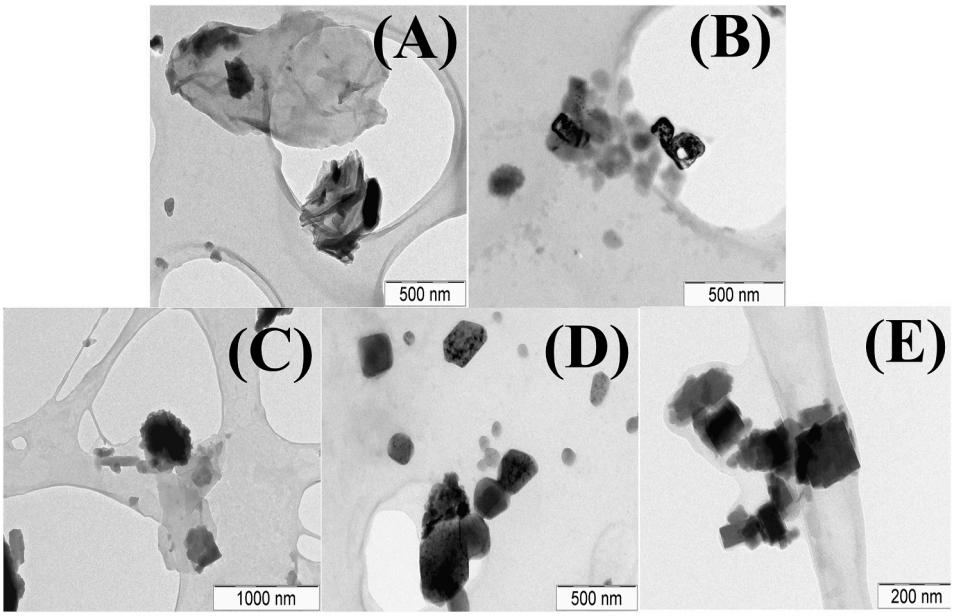

Fig. 3. TEM images of Co-POM/rGO (A), Fe-POM/rGO (B), Mn-POM/rGO (C), Ni-POM/rGO (D), and Cu-POM/rGO (E).

Ni-POM/rGO (0.068 V dec^{-1}), Co-POM/rGO (0.062 V dec^{-1}), and Mn-POM/rGO (0.066 V dec^{-1}) showed similar values of Tafel slope (b), while Tafel slope value of Fe-POM/rGO (0.074 V dec^{-1}) was somewhat higher, Table 1.

Several factors were considered to identify the best catalyst for OER. Firstly, the lower the Tafel slope, the better the electrocatalytic performance of a composite; still, Tafel slope values for Co-, Fe- and Ni-POM/rGO were quite similar. The difference appears then in the onset potential and current values at an overpotential of 400 mV. As shown in Table 1, Ni-POM/rGO presented the lowest onset potential, ca. 50 mV lower than that of Co-POM/rGO and ca. 100 mV lower than in the case of Mn-POM/rGO. Correspondingly, the current density at an overpotential of 400 mV delivered by Ni-POM/rGO was at least one order of magnitude higher than the other four composites. Thus, it was more than seven-fold higher than the current density recorded using Co-POM/rGO as the second-best performing material.

Previous theoretical and experimental study of OER in neutral media at tetra cobalt Weakley sandwich $[Co^{II}_4(H_2O)_2(B\text{-}\alpha\text{-}PW_9O_{34})_2]^{10-}$ (Co_4-WS) and its iron analogue $[Fe^{III}_4(H_2O)_2(B\text{-}\alpha\text{-}PW_9O_{34})_2]^{6-}$ (Fe_4-WS) examined the electronic effects governing their activity and revealed that Co-POMs display higher activity than the Fe analogues [49]. Furthermore, the study of POMs of different nuclearities reveals a minor influence of nuclearity on electrochemical performance. Weakley sandwich moieties show only somewhat better OER performance than the Keggin clusters [49]. Table 1 provides further comparison of OER performance of TM- and POM-based electrocatalysts reported in the literature. Still, the comparison should be taken with some care as different operational parameters (electrocatalyst's loading, electrolyte composition, scan rate, etc.) used across the literature reflect in different electrocatalysts' performance.

EIS measurements were carried out under OER polarization conditions to gain insight into the POM/rGO electrical properties. Electrolyte resistance (R_s) was similar in the case of all studied composites, with slight differences resulting from minor cell geometry and arrangement variations. Charge-transfer resistance at the electrode-electrolyte interface (R_{ct}), equivalent to the semicircle diameter in the Nyquist plots, was significantly different for the studied composites, Fig. 4B. Ni-POM/rGO exhibits R_{ct} of only 21.5 Ω compared to 207 Ω and 396 Ω in the case of Co-POM/rGO and Fe-POM/rGO, respectively. A decrease in R_{ct} with the potential increase could be seen for all studied composites (Fig. S1). The lowest R_{ct} in the case of Ni-POM/rGO can account for the highest current densities recorded and its overall best performance for OER.

Furthermore, double-layer capacitance (C_{dl}) measurements were done in a non-faradaic region, Fig. S2. C_{dl} value is directly proportional to the material's electrochemically active surface area (ECSA) and, thus, to the number of active sites. C_{dl} values for studied POM/rGO composites ranged from 0.386 to 0.715 mF cm^{-2}. Despite some differences, all composites show C_{dl} values of the same order of magnitude, indicating similar ECSA. It is important to note that the high-surface-area rGO contributes to the non-faradaic, capacitive currents and, consequently, affects ECSA determination. Still, the present estimation by the C_{dl} method is suitable for the ECSAs comparison, as all the studied materials contain rGO.

3.3. Optimising TM-POM/rGO composite composition

The results indicated Ni-POM/rGO as the best electrocatalyst for OER among the five studied composites. To determine the optimum composition of the POM/rGO composites, i.e., the ratio of POM to rGO that would lead to the highest electrocatalytic activity, the same set of measurements was carried out for different ratios (1:5, 2:4, 3:3, 4:2, 5:1) along with pristine Ni-POM and rGO. IrO_2, a benchmark noble-metal-based catalyst for OER, was also studied.

The LSVs revealed the highest current density for a ratio of Ni-POM:rGO 1:5. E_{onset} was found to increase in the order rGO (1.46 V) < Ni-POM:rGO (2:4) (1.50 V) < Ni-POM:rGO (1:5) (1.53 V) < Ni-POM:rGO (3:3) (1.54 V) < Ni-POM (1.54 V) < Ni-POM:rGO (5:1) (1.55 V) < Ni-POM:rGO (4:2) (1.55 V) < IrO_2 (1.56 V), Fig. 4C j_{400} was again the highest in the case of Ni-POM:rGO (1:5) and decreased in the order Ni-POM:rGO (1:5) (83.4 mA cm^{-2}) < Ni-POM (54.0 mA cm^{-2}) < rGO (49.4 mA cm^{-2}) < Ni-POM:rGO (3:3) (28.0 mA cm^{-2}) < Ni-POM:rGO (4:2) (27.6 mA cm^{-2}) < Ni-POM:rGO (2:4) (24.2 mA cm^{-2}) < IrO_2 (20.6 mA cm^{-2}) < Ni-POM:rGO (5:1) (15.0 mA cm^{-2}). All the materials showed increased activity with each additional LSV run (Fig. S3 illustrates the case of Ni-POM/rGO), possibly due to more Ni oxide forming during each LSV. Ni oxide is reported [50] to have higher activity for OER than metallic Ni, delivering increased current densities. The self-activation of catalysts based on Co-POM under OER conditions has been previously reported and attributed to Co-POM restructuration into amorphous Co oxide and/or hydroxide accompanied by increased active surface area [51,52].

Ni-POM/rGO (1:5) (354 mV), rGO (349 mV), and Ni-POM (355 mV)

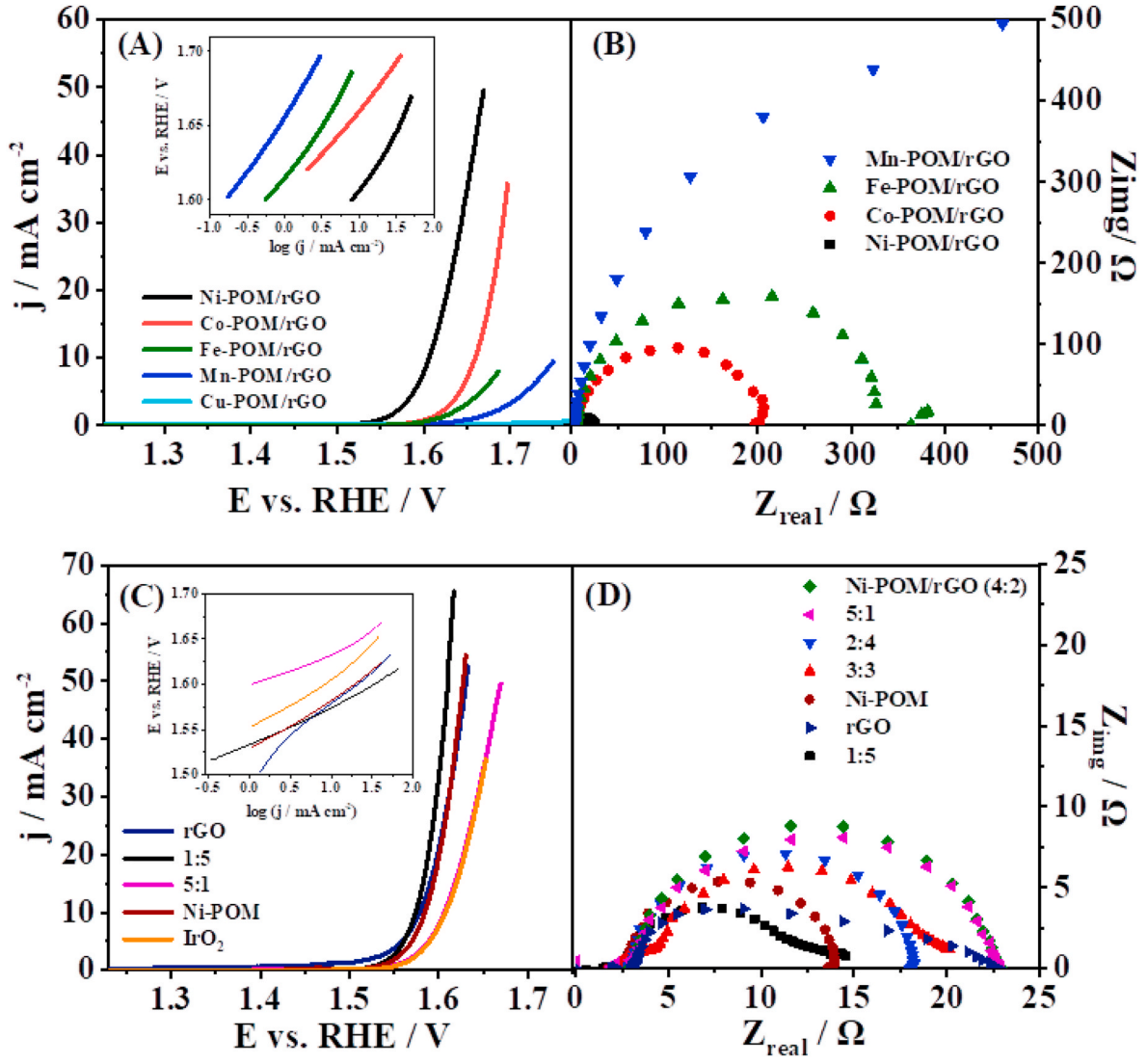

Fig. 4. Polarization curves (IR-corrected) of the five POM/rGO composites in 1 M KOH with the corresponding Tafel plots in inset (A), Nyquist plots of POM/rGO at 1.57 V (B), polarization curves (IR-corrected) of Ni-POM/rGO at different POM:rGO ratios (1:5 and 5:1), Ni-POM, rGO, and IrO_2 with the corresponding Tafel plots (average of three repetitions) in inset (C), Nyquist plots of Ni-POM/rGO at different POM:rGO ratios at 1.57 V (D).

exhibited similar overpotential to reach a current density of 10 mA cm^{-2}, lower than those of composites of other compositions. Next, Tafel analysis was performed, leading to the Tafel slope values presented in Table 2, where it can be seen that Ni-POM/rGO (1:5) has the lowest Tafel slope.

The main reaction parameters for OER are presented in Table 2. The Tafel slope of Ni-POM/rGO (1:5) is notably lower than that of other compositions. The activity of this composite could further be differentiated from the others by the high value of j_{400} and low overpotential to reach 10 mA cm^{-2}. Comparing the values obtained for the studied Ni-POM/rGO (1:5) (42 mV dec^{-1}) with the ones from the literature, it can be concluded that Ni-POM/rGO has an OER Tafel slope comparable to the best-performing materials reported, such as Fe_2Ni_2@MWCNT_N6 (45 mV dec^{-1}) [53], 2-CoFeW (43 mV dec^{-1}) [54] and ZIF-8@ZIF-67@POM (46 mV dec^{-1}) [55]. It also has a considerably lower Tafel slope than Co16-GeW9@NiF (84 mV dec^{-1}) [56] and PBA@POM (193 mV dec^{-1}) [57].

EIS measurements, Fig. 4D, revealed that Ni-POM/rGO (1:5) exhibited the lowest R_{ct} of only 10 Ω in comparison to 20 Ω in the case of Ni-POM/rGO (4:2), Ni-POM/rGO (5:1) and rGO. A decrease in R_{ct} with the potential increase could be observed for all POM:rGO ratios (Fig. S4). The lowest R_{ct} recorded with Ni-POM/rGO (1:5) can account for the highest current densities recorded and the overall best performance for OER. Furthermore, C_{dl} values for studied Ni-POM/rGO composites were of the same magnitude, ranging from 0.337 to 0.815 mF cm^{-2}, Fig. S5.

It should be pointed out that Ni-POM:rGO at the ratio of 1:5 exhibits the best performance not only among the POMs studied but also in comparison with the industry benchmark, IrO_2. For instance, j_{400} of Ni-POM:rGO (1:5) was ca. four times higher than that of IrO_2. Such high activity of Ni-POM/rGO can be attributed to the synergetic effect of the transition metal present, POM structure, high surface area, and high electrical conductivity of rGO. Namely, Ni and Co oxides are located on the left side of the OER volcano plot [58], and Ni and Co metals are on the left side of the ORR volcano plot [59]. This suggests they will bind oxygen intermediates slightly weaker than metals and oxides on top of the volcano plots, thus boosting the ORR/OER. The presence of POM enriched with protons and electrons augments the microenvironment effect (microenvironment around the active sites) [60]. Linking POMs to an appropriate conducting scaffold, such as rGO, results in reduced solubility, increased conductivity, and increased specific surface area of the composite. rGO has demonstrated scalability, native defects, and high conductivity. Enhanced performance of electrocatalysts containing rGO is generally ascribed to the high dispersion of electroactive

Table 1
Comparison of kinetic parameters of OER for POM/rGO (5:1) electrocatalysts and transition metal- or POM-based electrocatalysts reported in the literature.

Catalyst	b (mV dec^{-1})	E_{onset} vs. RHE (V)	η_{10} (mV)	j_{400} (mA cm^{-2})	Source
Cu-POM/rGO	–	–	–	0.2	This work
Mn-POM/rGO	66.4	1.656	–	0.4	This work
Fe-POM/rGO	74.5	1.615	467	1.7	This work
Co-POM/rGO	61.8	1.605	430	3.1	This work
Ni-POM/rGO	68.1	1.553	376	21.8	This work
Fe_2Ni_2@MWCNT_N6	45.0	1.575	360	–	[44]
Fe_4@MWCNT_N6	102	1.692	580	–	[44]
Ni_4@MWCNT_N6	54.0	1.595	460	–	[44]
ZIF-8@ZIF-67@POM	88.0	1.598	490	–	[45]
Co16-GeW9@NiF	84.0	–	370	–	[46]
PBA@POM	23.4	1.520	440	–	[47]
NiCoFe/TX/PW-CNTPE	83.0	1.396	210	–	[48]

b – Tafel slope; E_{onset} – onset potential; η_{10} – overpotential at current density of 10 mA cm^{-2}; j_{400} – current density at overpotential of 400 mV.

Table 2
OER kinetic parameters for different Ni-POM/rGO and IrO_2 electrocatalysts.

Catalyst	b (mV dec^{-1})	E_{onset} vs. RHE (V)	η_{10} (mV)	j_{400} (mA cm^{-2})
Pristine Ni-POM	49	1.54	355	54.0
Ni-POM:rGO 1:5	42	1.53	354	83.4
2:4	88	1.50	362	24.2
3:3	55	1.54	364	28.0
4:2	56	1.55	368	27.6
5:1	68	1.55	381	15.0
rGO	77	1.46	349	49.4
IrO_2	53	1.56	378	20.6

b – Tafel slope; E_{onset} – onset potential; η_{10} – overpotential at current density of 10 mA cm^{-2}; j_{400} – current density at overpotential of 400 mV.

component on rGO and the increased conductivity due to the presence of rGO. EIS has indeed shown effectively reduced contact and charge-transfer resistance of POMs on rGO. Moreover, the stability of these electrocatalysts is enhanced by the strong adhesion of POMs on rGO. The intimate POM-rGO contact boosts reaction kinetics and stability of nanocomposites. Two types of interactions between POMs and rGO have been identified: electron transfer and electrostatic interaction. Electrostatic interaction between POMs' corner shared metal oxygen site and the oxygen functional group on the graphene sheet have been identified. Additionally, a strong electron transfer interaction induced at the graphene sheets' defect site has been identified, altering the band gap energy [61]. The increased electrical conductivity leads to a decrease in the overpotential necessary to drive OER/ORR. The large specific surface area exposes a high number of active sites, including Ni or Co active sites [62]. Furthermore, the layered structure of Ni- and Co-POM/rGO composite facilitates the transport of active species within the electrocatalysts' porous structure to active sites, enhances charge transfer, and enables the escape of generated gas (cleaning the active sites from gas bubbles).

Another parameter vital for commercial applications is the catalyst price. The prices of each catalyst per unit current were calculated based on prices available online, Table 3 [63]. By including in the calculations the current at an overpotential of 400 mV, it can be seen that Ni-POM/rGO at all ratios is cheaper per unit of current produced than IrO_2. It is also essential to note that both the rGO and POMs studied herein were produced "in-house", meaning that both costs are substantially lower than those of their commercial counterparts. As the synthesis process is relatively simple and uses cheap, sustainable reagents, its scale-up to the industrial level would be straightforward. From all this, it is concluded that the Ni-POM/rGO studied here outperforms the current benchmark IrO_2 electrocatalyst in every aspect for OER.

Table 3
Materials' prices per unit of current.

Catalyst	Price per current ($ A^{-1})
rGO	228
POM:rGO 1:5	113
2:4	311
3:3	202
4:2	137
5:1	128
IrO_2	410

3.4. Study of POM/rGO composites as electrocatalysts for ORR

To investigate the potential use of POM/rGO composites as bifunctional electrocatalysts for oxygen electrodes in MABs, i.e., for both OER and ORR, the performance of POM/rGO was next evaluated under the ORR polarization conditions, Fig. S6. ORR studies focused on Ni-POM/rGO (1:5) and Co-POM/rGO (1:5) as the best and the second-best electrocatalysts for OER among the five tested composites. A comparison of the current densities recorded in N_2- and O_2-saturated solutions shows an apparent increase in the presence of O_2 in the case of both composites, corresponding to the oxygen reduction. Furthermore, Co-POM/rGO (1:5) exhibited higher performance under ORR polarization conditions than Ni-POM/rGO (1:5), with current densities recorded using Co-POM/rGO being double those of Ni-POM/rGO, Fig. 5A–C and Fig. S6. Onset potential was determined as the intersection point of the tangents to the baseline and the rising current density part of CV curves at 1600 rpm and found to be 0.826 and 0.719 V for Co-POM/rGO and Ni-POM/rGO, respectively. Thus, Co-POM/rGO (1:5) showed more than 100 mV more positive onset potential than Ni-POM/rGO (1:5), corroborating its higher activity for ORR. Additionally, half-wave potential ($E_{1/2}$), as another widely-used indicator for the evaluation of the electrocatalytic activity of new electrode materials for ORR, was found to have ca. 90 mV more positive value for Co-POM/rGO (1:5) (0.711 V) compared to Ni-POM/rGO (1:5) (0.620 V). ORR Tafel analysis revealed a lower absolute Tafel slope value in the case of Co-POM/rGO (−165 mV dec^{-1}) than Ni-POM/rGO (−175 mV dec^{-1}), further demonstrating its better ORR performance.

Koutecký-Levich analysis was next performed using background-corrected data at three different potentials. The number of electrons (n) transferred during ORR was determined from the slope of Koutecký-Levich plots (j^{-1} vs. $\omega^{-1/2}$), Fig. 5B–D. ORR n values for Co-POM/rGO (1:5) ranged from 2.6 to 2.7, suggesting that oxygen reduction proceeds by the 2-electron pathway (Eq. (1)) assisted by further reduction of HO_2^- (Eq. (2)) or its disproportionation (Eq. (3)) A mixed mechanism instead of the envisioned 4-electron pathway was also reported for ORR at Fe_4@MWCNT_N6, Ni_4@MWCNT_N6, and Fe_2Ni_2@MWCNT_N6 with a number of electrons exchanged of 2.9, 2.7, and 3.2, respectively [51]. Similarly, the number of exchanged electrons of 2.77–3.8 was determined for ORR at tetra cobalt sandwich polyoxometalate $[Co_4(H_2O)_2(PW_9O_{34})_2]^{10-}$ and polyvinyl butyl imidazolium supported on different carbon supports (Vulcan carbon, Vulcan carbon – polypyrrole and nitrogen-doped carbon nanotubes) [64]. On the other hand, the n value for Ni-POM/rGO (1:5) was evaluated to range from 1.7 to 1.8.

$$O_2 + H_2O + 2e^- \leftrightarrow HO_2^- + OH^- \quad E^0 = -0.076 \text{ V vs. SHE} \tag{1}$$

$$HO_2^- + H_2O + 2e^- \leftrightarrow 3OH^- \quad E^0 = 0.878 \text{ V vs. SHE} \tag{2}$$

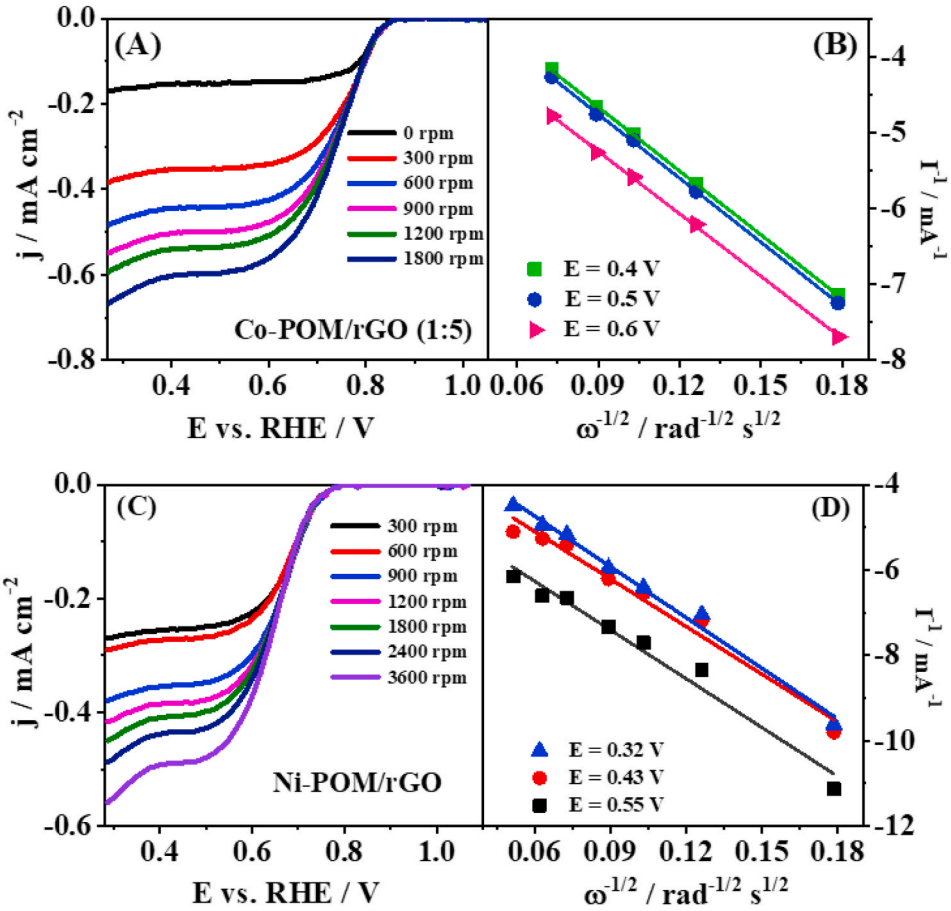

Fig. 5. LSVs of (A) Co-POM/rGO (1:5) and (C) Ni-POM/rGO at different electrode rotation rates with (B,D) the corresponding Koutecký-Levich analysis (average of three repetitions) at three different potentials.

$$2HO_2^- \leftrightarrow 2OH^- + O_2 \quad (3)$$

Table 4 summarizes the determined kinetic parameters of ORR at Co-POM/rGO (1:5) and Ni- POM/rGO (1:5). Notably, more positive onset potential (ca. 105 mV difference) and half-wave potential (ca. 90 mV difference), slightly lower Tafel slope and higher number of electrons exchanged demonstrate the superior performance of Co-POM/rGO for ORR compared to Ni-POM/rGO. Table 4 further provides comparison with performance towards ORR in alkaline media of similar TM- or POM-based electrocatalysts reported in the literature.

Finally, the initial chronoamperometric study revealed stable performance of Co-POM/rGO under both oxygen reduction and evolution conditions, Fig. 6. Small variations in current density due to intense bubbling could be seen. Continuous cycling (1000 cycles) was also performed within a wide potential window encompassing both ORR and OER potential region, Fig. S7. XRD patterns taken before and after the cycling test revealed no change in the materials' structure confirming the stable performance of TM-POM/rGO electrocatalysts during ORR/OER. Fig. S7 illustrates case of Co-POM/rGO; both difractograms displayed a diffraction peak at 25° and a low-intensity peak at 43.5° corresponding to the reflections from the C(002) and C(100) crystal plane [69].

High activity as well as stability in alkaline conditions underlines that these composite materials, primarly Co-POM/rGO, are promising for oxygen electrode reactions. To further evaluate their performance, these composite materials could be inspected in a MAB. Initial studies involving Al-air battery have been done (Fig. S8), but more in-depth studies of MAB construction were outside the scope of this study.

Table 4
Kinetic parameters of ORR at Co-POM/rGO (1:5), Ni-POM/rGO (1:5) and some catalysts reported in the literature.

Catalyst	b (mV dec^{-1})	n	j_d (mA cm^{-2})	E_{onset} vs. RHE (V)	$E_{1/2}$ vs. RHE (V)	Source
Co-POM/rGO	165	2.6–2.7	1.07	0.826	0.711	This work
Ni-POM/rGO	175	1.7–1.8	0.82	0.719	0.620	This work
Fe_4@MWCNT_N6	35.4	2.9	−3.19	0.800	–	[65]
Ni_4@MWCNT_N6	34.7	2.7	−3.20	0.800	–	[65]
Fe_2Ni_2@MWCNT_N6	37.9	3.2	−3.66	0.810	–	[65]
Pd/rPOM	−72	3.9	–	1.087	–	[66]
Pd_8Ni_2/rGO-POM	59.7	3.9	−1.73	0.834	–	[67]
PVIM–CoPOM	–	2.5	−3.5	0.840	–	[68]
PVIM–CoPOM/NCNT	–	3.8	−5.2	0.990	–	[68]

b – Tafel slope; n – number of exchanged electrons; j_d – diffusion-limited current density; E_{onset} – onset potential; $E_{1/2}$ – half-wave potential.

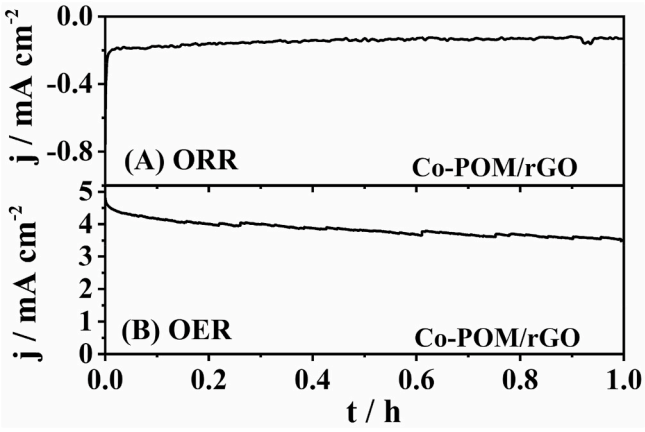

Fig. 6. Chronoamperometric measurements using Co-POM/rGO under (A) oxygen reduction and (B) oxygen evolution conditions.

4. Conclusions

Five transition metal-polyoxometalates (TM-POMs) were combined with reduced graphene oxide (rGO) and assessed as bifunctional electrocatalysts for air electrodes in metal-air batteries (MABs). Their Fourier-transform infrared spectra displayed characteristic bands of POM and rGO structures, and energy dispersive X-ray spectra confirmed the presence of five different metals (Ni, Co, Mn, Cu, Fe) within the structures. Furthermore, X-ray diffraction, Raman spectroscopy and transimission electron microscopy analysis revealed POMs of Kenning structure with nanolamellae-like morphology and multi-layered graphene sheets of rGO.

Ni-POM/rGO was the best candidate for oxygen evolution reaction (OER), and further studies showed that the optimal Ni-POM:rGO ratio was 1:5. The performance of this catalyst was auspicious (Tafel slope as low as 42 mV dec^{-1}, overpotential at 10 mA cm^{-2} of 354 mV and current density at 400 mV overpotential as high as 83.4 mA cm^{-2}), being even higher than that of IrO_2, the catalyst currently considered the best for this reaction. It is also important to note that although Co-POM/rGO was not as good as Ni-POM, it came second for OER. In terms of oxygen reduction reaction (ORR), Co-POM/rGO demonstrated the highest performance with a Tafel slope of 165 mV dec^{-1}, half-wave potential of 0.711 V and a mixed 2- and 4-electron ORR mechanism. Such high performance of TM-POMs combined with rGO results from the presence of transition metals in high oxidation states, the high electrical conductivity of rGO (and therefore low charge-transfer resistance at the electrode/electrolyte interface), high specific surface area (thus, a higher number of active sites), as well as high porosity (facilitating the mass transfer). Moreover, these non-noble metal electrocatalysts exhibited stability in alkaline media with no change in their structure unlike number of POMs reported in the literature. Thus the present study offers a practicable strategy to rational design and scalable production of economically viable electrocatalysts for efficient energy conversion and storage.

CRediT authorship contribution statement

Filipe.M.B. Gusmão: Formal analysis, Investigation, Visualization, Writing – original draft. **Teodora Đurić:** Formal analysis, Investigation. **Jadranka Milikić:** Formal analysis, Investigation, Visualization, Writing – original draft. **Kristina Radinović:** Supervision, Visualization, Writing – original draft. **Diogo.M.F. Santos:** Supervision, Writing – review & editing. **Dalibor Stanković:** Conceptualization, Supervision, Writing – review & editing. **Biljana Šljukić:** Conceptualization, Funding acquisition, Project administration, Supervision, Visualization, Writing – review & editing.

Declaration of competing interes

The authors declare that they have no known competing financial interests or personal relationships that could have appeared to influence the work reported in this paper.

Acknowledgments

Fundação para a Ciência e a Tecnologia (FCT, Portugal) is acknowledged for funding EXPL/EQU-EQU/0517/2021 project as well as research contract in the scope of programmatic funding UIDP/04540/2020 (D.M.F. Santos) and contract no. IST-ID/156–2018 (B. Šljukić).

Appendix A. Supplementary data

Supplementary data to this article can be found online at https://doi.org/10.1016/j.ijhydene.2024.05.229.

References

[1] United Nations website, https://gadebate.un.org/en/77/secretary-general-united-nations (visited on 1/October/2022).
[2] Islam J, Anwar R, Shareef M, Zabed HM, Sahu JN, Qi X, Khandaker MU, Ragauskas A, Boukhris I, Rahman MR, Islam Chowdhury F. Rechargeable metal-metal alkaline batteries: recent advances, current issues and future research strategies. J Power Sources 2023;563:232777. https://doi.org/10.1016/J.JPOWSOUR.2023.232777.
[3] Buckingham R, Asset T, Atanassov P. Aluminium-air batteries: a review of alloys, electrolytes and design. J Power Sources 2021;498:229762. https://doi.org/10.1016/J.JPOWSOUR.2021.229762.
[4] Yavari Z, Shaybani S, Saffari J, Kerman K, Noroozifar M. Stoichiometry influence of oxide support on the catalytic efficiency of nano-palladium towards CH_3OH electrooxidation. Chemical Paper 2021;75:2317–29. https://doi.org/10.1007/s11696-020-01485-8.
[5] Pegis M, McKeown B, Kumar N, Lang K, Wasylenko D, Zhang P, Simone Raugei S, Mayer J. Homogenous electrocatalytic oxygen reduction rates Correlate with reaction overpotential in acidic organic solutions. ASC Cent. Sci. 2016;2(11):850–6. https://doi.org/10.1021/acscentsci.6b00261.
[6] Najmeh S, Shervin S, Meissam N, Masoumeh T. Simultaneous determination of Dopamine, Acetaminophen and Xanthine by modified carbon Ceramic Microelectrode with Nanosized $LaFe_{0.2}Ni_{0.8}O_3$ perovskite. Analytical & Bioanalytical Electrochemistry 2018;10(12):1525–35.
[7] Mamaca N, Mayousse E, Arrii-Clacens S, Napporn T, Servat K, Guillet N, Kokoh K. Electrochemical activity of ruthenium and iridium based catalysts for oxygen evolution reaction. Appl Catal, B: Enviromental 2012;12:376–80. https://doi.org/10.1016/j.micromeso.2021.111670. 111-112.
[8] Rabiee N, Atarod M, Tavakolizadeh M, Asgari S, Rezaei M, Akhavan O, Pourjavadi A, Jouyandeh M, Lima E, Mashhadzadeh AH, Ehsani A, Ahmadi S, Reza Saeb M. Green metal-organic frameworks (MOFs) for biomedical applications. Microporous Mesoporous Mater 2022;335:111670. https://doi.org/10.1016/j.micromeso.2021.111670.
[9] Wang C, Markovic N, Stamenkovic V. Advanced platinum alloy electrocatalysts for the oxygen reduction reaction. ASC Catalyst 2012;2(5):891–8. https://doi.org/10.1021/cs3000792.
[10] Marini E, Jörissen L, Brimaud S. Rational design of a low-cost, durable and efficient bifunctional oxygen electrode for rechargeable metal-air batteries. J Power Sources 2021;482:228900. https://doi.org/10.1016/J.JPOWSOUR.2020.228900.
[11] Gusmão FMB, Mladenović D, Radinović K, Santos DMF, Šljukić B. Polyoxometalates as electrocatalysts for electrochemical energy conversion and storage. Energies 2022;15(23):9021. https://doi.org/10.3390/en15239021.
[12] Cherevan A, Nandan S, Roger I, Liu R, Streb C, Eder D. Polyoxometalates on functional substrates: Concepts, Synergies, and future Perspectives. Adv Sci 2020;7:1903511. https://doi.org/10.1002/advs.201903511.
[13] Wang H, Kawasaki N, Yokoyama T, Yoshikawa H, Awaga K. Molecular cluster batteries of nano-hybrid materials between Keggin POMs and SWNTs. Dalton Trans 2012;41(33):9863. https://doi.org/10.1039/c2dt30603d.
[14] Guzel M, Torlak Y, Choi H, Ak M. "Perfect match" of the carbazole-based conducting polymer and polyoxometalate nanocomposite components for enhanced optical and electrical properties. Eur Polym J 2023;186:111857. https://doi.org/10.1016/J.EURPOLYMJ.2023.111857.
[15] Liu Y, Zhang J, Lu S, Xiang Y. Polyoxometalate-based electrolyte materials in redox flow batteries: current trends and emerging opportunities. Materials Reports: Energy 2022;2(2):100094. https://doi.org/10.1016/J.MATRE.2022.100094.
[16] Gao Y, Choudhari M, Such G, Ritchie C. Polyoxometalates as chemically and structurally versatile components in self-assembled materials. Chem Sci 2022;13:2510. https://doi.org/10.1039/d1sc05879g.
[17] Zhang Y, Li Y, Guo H, Guob Y, Song R. Recent advances in polyoxometalate-based materials and their derivatives for electrocatalysis and energy storage. Mater Chem Front 2024;8:732–68. https://doi.org/10.1039/D3QM01000G.

[18] Fan X, Zhang J, Yang Y, Xia D, Dong Y, Qiu L, Wang JQ, Cao W, Wang W, Hu B, Fan R. New insight into the grafted transition metal ions in trilacunary Keggin polyoxometalates dopants for efficient and stable perovskite solar cells. J Power Sources 2021;504:230073. https://doi.org/10.1016/J.JPOWSOUR.2021.230073.

[19] Zeb Z, Huang Y, Chen L, Zhou W, Liao M, Jiang Y, Li H, Wang L, Wang L, Wang H, Wei T, Zang D, Fan Z, Wei Y. Comprehensive overview of polyoxometalates for electrocatalytic hydrogen evolution reaction. Coord Chem Rev 2023;482:215058. https://doi.org/10.1016/J.CCR.2023.215058.

[20] Wang H, Hamanaka S, Nishimoto Y, Irle S, Yokoyama T, Yoshikawa H, Awaga K. In Operando X-ray absorption fine structure studies of polyoxometalate molecular cluster batteries: polyoxometalates as electron Sponges. J Am Chem Soc 2012;134 (10):4918–24. https://doi.org/10.1021/ja2117206.

[21] Kawasaki N, Wang H, Nakanishi R, Hamanaka S, Kitaura R, Shinohara H, Yokoyama T, Yoshikawa H, Awaga K. Nanohybridization of polyoxometalate clusters and single-Wall carbon nanotubes: applications in molecular cluster batteries. Angew Chem Int Ed 2011;50(15):3471–4. https://doi.org/10.1002/anie.201007264.

[22] López X, Fernández JA, Poblet JM. Redox properties of polyoxometalates: new insights on the anion charge effect. Dalton Trans 2006;9:1162–7. https://doi.org/10.1039/B507599H.

[23] López X, Bo C, Poblet JM. Electronic properties of polyoxometalates: electron and proton Affinity of mixed-Addenda Keggin and Wells−Dawson anions. J Am Chem Soc 2002;124(42):12574–82. https://doi.org/10.1021/ja020407z.

[24] Araújo H, Šljukić B, Gago S, Santos D. The current state of transition metal-based electrocatalysts (oxides, alloys, POMs, and MOFs) for oxygen reduction, oxygen evolution, and hydrogen evolution reactions. Front Energy Res 2024;12.

[25] Imani A, Ojani R, Raoof J. Facile synthesis of polyoxometalate-based composite with doped ternary NiCoFe cations as electrocatalyst for oxygen evolution reaction. Int J Hydrogen Energy 2021;46(1):449–57. https://doi.org/10.1016/j.ijhydene.2020.09.215.

[26] Xue X, Yu F, Jian-Gang Li J, Bai G, Yuan H, Hou J, Peng B, Chen L, Yuen M, Wang G, Wang F, Wang C. Polyoxometalate intercalated NiFe layered double hydroxides for advanced water oxidation. Int J Hydrogen Energy 2020;45(3): 1802–9. https://doi.org/10.1016/j.ijhydene.2019.11.038.

[27] Song J, Zhu P, Ma W, Li Y. PW_6Mo_6/ZIF-67@NF composite with exposed Co nodes as efficient oxygen evolution reaction electrocatalyst. Int J Hydrogen Energy 2024; 51:327–37. https://doi.org/10.1016/j.ijhydene.2023.10.031.

[28] Lei J, Fan X, Liu T, Xu P, Hou Q, Li K, Yuan R, Zheng MS, Dong QF, Chen JJ. Single-dispersed polyoxometalate clusters embedded on multilayer graphene as a bifunctional electrocatalyst for efficient Li-S batteries. Nat Commun 2022;13:202. https://doi.org/10.1038/s41467-021-27866-5.

[29] Clemente-Juan JM, Coronado E, Galán-Mascarós JR, Gómez-García CJG. Increasing the nuclearity of magnetic polyoxometalates. Syntheses, structures, and magnetic properties of salts of the Heteropoly Complexes [Ni3(H2O)3(PW10O39) H2O]7-, [Ni4(H2O)2(PW9O34)2]10-, and [Ni9(OH)3(H2O)6(HPO4)2(PW9O34) 3]16-. Inorg Chem 1999;38:55–63.

[30] Dehghani Sanij F, Balakrishnan P, Su H, Khotseng L, Xu Q. Fabrication of polyoxometalate-modified palladium–nickel/reduced graphene oxide alloy catalysts for enhanced oxygen reduction reaction activity. RSC Adv 2021;11(62): 39118–29. https://doi.org/10.1039/D1RA06936E.

[31] Ross N, Civilized Nqakala N. Electrochemical determination of hydrogen peroxide by a Nonenzymatic Catalytically enhanced Silver-iron (III) oxide/polyoxometalate/reduced graphene oxide modified glassy carbon electrode. Anal Lett 2020;53(15):2445–64. https://doi.org/10.1080/00032719.2020.1745223.

[32] Khodadadi Dizaji A, Mortaheb HR, Mokhtarani B. Preparation of supported catalyst by adsorption of polyoxometalate on graphene oxide/reduced graphene oxide. Mater Chem Phys 2017;199:424–34. https://doi.org/10.1016/j.matchemphys.2017.07.016.

[33] Tarlani A, Abedini M, Nemati A, Khabaz M, Amini MM. Immobilization of Keggin and Preyssler tungsten heteropolyacids on various functionalized silica. J Colloid Interface Sci 2006;303(1):32–8. https://doi.org/10.1016/j.jcis.2006.07.024.

[34] Karimi Z, Mahjoub AR, Harati SM. Polyoxometalate-based hybrid mesostructured catalysts for green epoxidation of olefins. Inorg Chim Acta 2011;376(1):1–9. https://doi.org/10.1016/J.ICA.2011.05.024.

[35] Yokuş ÖA, Kardaş F, Akyildirim O, Eren T, Atar N, Yola ML. Sensitive voltammetric sensor based on polyoxometalate/reduced graphene oxide nanomaterial: Application to the simultaneous determination of l-tyrosine and l-tryptophan. Sensor Actuator B Chem 2016;233:47–54. https://doi.org/10.1016/J.SNB.2016.04.050.

[36] Yola ML, Atar N, Eren T, Karimi-Maleh H, Wang S. Sensitive and selective determination of aqueous triclosan based on gold nanoparticles on polyoxometalate/reduced graphene oxide nanohybrid. RSC Adv 2015;5(81): 65953–62. https://doi.org/10.1039/C5RA07443F.

[37] Yin Q, Xu Z, Lian T, Musaev DG, Hill CL, Geletii YV. Tafel slope Analyses for Homogeneous catalytic reactions. Catalysts 2021;11(1):87. https://doi.org/10.3390/catal11010087.

[38] Alam SN, Sharma N, Kumar L. Synthesis of graphene oxide (GO) by modified Hummers method and its thermal reduction to Obtain reduced graphene oxide (rGO). Graphene 2017;6:1–18. https://doi.org/10.4236/graphene.2017.61001.

[39] Calizo I, Balandin AA, Bao W, Miao F, Lau CN. Temperature Dependence of the Raman spectra of graphene and graphene Multilayers. Nano Letter 2007;7(9): 2645–9. https://doi.org/10.1021/nl071033g.

[40] Akhavan O. Bacteriorhodopsin as a superior substitute for hydrazine in chemical reduction of single-layer graphene oxide sheets. Carbon 2015;81:158–66. https://doi.org/10.1016/j.carbon.2014.09.044.

[41] Omachi H, Inoue T, Hatao S, Shinohara H, Criado A, Yoshikawa H, Syrgiannis Z, Prato M. Concise, single-step synthesis of Sulfur-enriched graphene: Immobilization of molecular clusters and battery applications. Angew Chem Int Ed 2020;59:7836–41. https://doi.org/10.1002/anie.201913578.

[42] Kaur J, Anand K, Anand K, Singh RC. WO_3 nanolamellae/reduced graphene oxide nanocomposites for highly sensitive and selective acetone sensing. J. Mater Science 2018;53:12894–907. https://doi.org/10.1007/s10853-018-2558-z.

[43] Liu Q, Wang X. Polyoxometalate clusters: Sub-nanometer building blocks for construction of advanced materials. Matter 2020;2(4):816–41. https://doi.org/10.1016/j.matt.2020.01.020.

[44] Marques IS, Jarrais B, Mbomekallé. I-M, Anne-Lucie Teillout A-L, Oliveira P, Freire C, Diana M, Fernandes DM. Synergetic effects of mixed-metal polyoxometalates@carbon-based composites as electrocatalysts for the oxygen reduction and the oxygen evolution reactions. Catalysts 2022;12(4):440. https://doi.org/10.3390/catal12040440.

[45] Wang Y, Wang Y, Zhang L, Liu C-S, Pang H. Core–shell-type ZIF-8@ZIF-67@POM hybrids as efficient electrocatalysts for the oxygen evolution reaction. Inorg. Chem. Front. 2019;2019(6):2514–20. https://doi.org/10.1039/c9qi00798a.

[46] Ahmeda T, Asghara MA, Alib A, Akhtera Z, Saqib Alia S, Ullaha I, Nisare T, Wagnere V, Touseefa S, Hussaina A, Haidera A. High-nuclearity cobalt(II)-containing polyoxometalate anchored on nickel foam as electrocatalyst for electrochemical water oxidation studies. J. Alloys Compd. 2022;909:164709. https://doi.org/10.1016/j.jallcom.2022.164709Z. 2022.

[47] Wang Y, Wang Y, Zhang L, Liu C-S, Pang H. PBA@POM hybrids as efficient electrocatalysts for the oxygen evolution reaction. Chem. Asian J. 2019;14:2790–5. https://doi.org/10.1002/asia.201900791N.

[48] Imani AH, Ojani R, Raoof J-B. Facile synthesis of polyoxometalate-based composite with doped ternary NiCoFe cations as electrocatalyst for oxygen evolution reaction. Int. J. Hydrogen Energy 2021;46:449–57. https://doi.org/10.1016/j.ijhydene.2020.09.215K. 2021.

[49] Azmani K, Besora M, Soriano-Lopez J, Landolsi M, Teillout A-L, Oliveira P, Mbomekall I-M, Poblet JM, Galan-Mascaros J-R. Understanding polyoxometalates as water oxidation catalysts through iron vs. cobalt reactivity. Chem Sci 2021;12: 8755–66.

[50] Steimecke M, Seiffarth G, Schneemann C, Oehler F, Förster S, Bron M. Higher-valent nickel oxides with Improved oxygen evolution activity and stability in alkaline media prepared by high-Temperature Treatment of $Ni(OH)_2$. ACS Catal 2020;10(6):3595–603. https://doi.org/10.1021/acscatal.9b04788.

[51] Gong R, Gao D, Liu R, Sorsche D, Biskupek J, Kaiser U, Rau S, Streb C. Self-activation of a polyoxometalate-Derived composite electrocatalyst for the oxygen evolution reaction. ACS Appl Energy Mater 2021;4(11):12671–6. https://doi.org/10.1021/acsaem.1c02399.

[52] Tariq I, Asghar MA, Ali A, Badshah A, Abbas SM, Iqbal W, Zubair M, Haider A, Zaman S. Surface Reconstruction of cobalt-based polyoxometalate and CNT Fiber composite for efficient oxygen evolution reaction. Catalysts 2022;12(10):1242. https://doi.org/10.3390/catal12101242.

[53] Marques IS, Jarrais B, Mbomekallé I-M, Teillout A-L, de Oliveira P, Freire C, Fernandes DM. Synergetic effects of mixed-metal Polyoxometalates@Carbon-based composites as electrocatalysts for the oxygen reduction and the oxygen evolution reactions. Catalysts 2022;12(4):440. https://doi.org/10.3390/catal12040440.

[54] Yu L, Du X, Ding Y, Chen H, Zhou P. Efficient visible light-driven water oxidation catalyzed by an all-inorganic copper-containing polyoxometalate. Chem Commun 2015;51(98):17443–6. https://doi.org/10.1039/C5CC07119D.

[55] Wang Y, Wang Y, Zhang L, Liu C-S, Pang H. Core-shell-type ZIF-8@ZIF-67@POM hybrids as efficient electrocatalysts for the oxygen evolution reaction. Inorg Chem Front 2019;6(9):2514–20. https://doi.org/10.1039/C9QI00798A.

[56] Ahmed T, Asghar MA, Ali A, Akhter Z, Ali S, Ullah I, Nisar T, Wagner V, Touseef S, Hussain A, Haider A. High-nuclearity cobalt(II)-containing polyoxometalate anchored on nickel foam as electrocatalyst for electrochemical water oxidation studies. J Alloys Compd 2022;909:164709. https://doi.org/10.1016/j.jallcom.2022.164709.

[57] Wang Y, Wang Y, Zhang L, Liu C, Pang H. PBA@POM hybrids as efficient electrocatalysts for the oxygen evolution reaction. Chemistry – An Asian Journal, asia 2019:201900791. https://doi.org/10.1002/asia.201900791.

[58] Man IC, Su H, Calle-Vallejo F, Hansen HA, Martínez JI, Inoglu NG, Kitchin J, Jaramillo TF, Nørskov JK, Rossmeisl J. Universality in oxygen evolution electrocatalysis on oxide surfaces. ChemCatChem 2011;3(7):1159–65. https://doi.org/10.1002/cctc.201000397.

[59] Nørskov JK, Rossmeisl J, Logadottir A, Lindqvist L, Kitchin JR, Bligaard T, Jónsson H. Origin of the overpotential for oxygen reduction at a Fuel-cell Cathode. J Phys Chem B 2004;108(46):17886–92. https://doi.org/10.1021/jp047349j.

[60] Liu R, Zhang G, Cao H, Zhang S, Xie Y, Haider A, Kortz U, Chen B, Dalal NS, Zhao Y, Zhi L, Wu C-X, Yan L-K, Su Z, Keita B. Enhanced proton and electron reservoir abilities of polyoxometalate grafted on graphene for high-performance hydrogen evolution. Energy Environ Sci 2016;9(3):1012–23. https://doi.org/10.1039/C5EE03503A.

[61] Cherevan AS, Nandan SP, Roger I, Liu R, Streb IC, Eder D. Polyoxometalates on functional substrates: concepts, synergies, and future perspectives. Adv. Sci. 2020; 7:1903511. https://doi.org/10.1002/advs.201903511.

[62] Zdolšek N, Vujković M, Metin Ö, Brković S, Jocić A, Dimitrijević A, Trtić-Petrović T, Šljukić B. Boosting electrocatalysis of oxygen reduction and evolution reactions with cost-effective cobalt and nitrogen-doped carbons prepared by simple carbonization of ionic liquids. Int J Hydrogen Energy 2022;47(33):14847–58. https://doi.org/10.1016/j.ijhydene.2022.02.225.

[63] Sigma Aldrich, https://www.sigmaaldrich.com (visited on 1/September/2022.).

[64] Nagaiah TC, Gupta D, Adhikary SD, Kafle A, Mandal D. Tuning polyoxometalate composites with carbonaceous materials towards oxygen bifunctional activity. J Mater Chem A 2021;9:9228–37. https://doi.org/10.1039/D0TA10423J.
[65] Marques I, Jarrais B, Mbomekallé IM, Teillout AL, Oliveira P, Freire C, Fernandes DM. Synergetic effects of mixed-metal Polyoxometalates@Carbon-based composites as electrocatalysts for the oxygen reduction and the oxygen evolution reactions. Catalysts 2022;12:440. https://doi.org/10.3390/catal12040440.
[66] Xie X, Nie Y, Chen S, Ding W, Qi X, Li L, Wei Z. A catalyst superior to carbon-supported-platinum for promotion of the oxygen reduction reaction: reduced-polyoxometalate supported palladium. J Mater Chem A 2015;3:13962–9. https://doi.org/10.1039/C5TA02196K.
[67] Sanij FD, Balakrishnan P, Su H, Khotseng L, Qian Xu Q. Fabrication of polyoxometalate-modified palladium–nickel/reduced graphene oxide alloy catalysts for enhanced oxygen reduction reaction activity. RSC Advance 2021;11: 39118–29. https://doi.org/10.1039/D1RA06936E.
[68] Nagaiah T, Gupta D, Adhikary SD, Kaflea A, Mandal D. Tuning polyoxometalate composites with carbonaceous materials towards oxygen bifunctional activity. J Mater Chem A 2021;9:9228–37. https://doi.org/10.1039/D0TA10423J.
[69] Milikić J, Nastasić A, Rakočević L, Radinović K, Stojadinović S, Stanković D, Šljukić B. FeM/rGO (M = Ni and Cu) as bifunctional oxygen electrode. Fuel 2024; 368:131654. https://doi.org/10.1016/j.fuel.2024.131654.